Acta Materialia 194 (2020) 378–386

Contents lists available at ScienceDirect

Acta Materialia

journal homepage: www.elsevier.com/locate/actamat

Full length article

Ductility limit diagrams for superplasticity and forging of high temperature polycrystalline materials

Wei Zhang[a,b], Yanfei Gao[a,*], Zhili Feng[b,*], Xin Wang[c], Siyu Zhang[c], Lan Huang[c], Zaiwang Huang[c,*], Liang Jiang[d,*]

[a] Department of Materials Science and Engineering, University of Tennessee, Knoxville, TN 37996, USA
[b] Materials Science and Technology Division, Oak Ridge National Laboratory, Oak Ridge, TN 37831, USA
[c] State Key Laboratory of Power Metallurgy, Central South University, Changsha 410083, China
[d] Institute for Advanced Studies in Precision Materials, Yantai University, Yantai 264005, China

ARTICLE INFO

Article History:
Received 18 January 2020
Revised 21 April 2020
Accepted 22 April 2020
Available online 10 May 2020

Keywords:
Superplasticity limit diagram
Forming limit diagram
High temperature alloys
Intergranular cavitation
Necking
Shear band

ABSTRACT

A mechanistic understanding of the ductility limit diagrams is of critical importance, but it still remains elusive for a multitude of high temperature materials processing techniques, such as superplastic forming and hot forging. The relevant failure modes for the former are necking at high strain rates and intergranular cavitation at low strain rates, while those for the latter include the competition between longitudinal fracture and shear band. The comparison between the Arrhenius processes for grain boundary diffusion and grain interior creep defines a length scale that dictates whether the grain boundary cavity growth is diffusive or creep-constrained. A quantitative assessment of these damage evolution processes leads to the delineation of the dominant parametric spaces for individual failure modes, and thus superplasticity and forging limit diagrams are derived and compared to available experiments in literature.

1. Introduction

The integration between metallurgy and mechanics has made great improvements of mechanical properties of advanced structural materials, especially their degradation resistance under extreme thermal, mechanical, corrosive, and irradiation environments [1–4]. Not only we now have the know-how to design novel alloys for jet engines and gas turbines at unprecedented operation temperatures, but also the mechanistic understanding of their deformation and failure mechanisms provides open opportunities to develop new processing techniques. For example, superplasticity can be realized in many commercial alloys for metal forming, and hot forging has been widely used in manufacturing turbine disks and other high-temperature components. Despite the above achievements and widespread applications, a technical hurdle is the surprising lack of mechanism-based and predictive diagrams for the ductility limit, as schematically illustrated by the representative experiments in Fig. 1. Superplasticity limit is shown in Fig. 1(a), where a maximum ductility is observed at the intermediate strain rate. According to Nieh et al. [3], the ductility limit in superplasticity is commonly explained by the necking instability, as governed by the Hart condition of

$$\frac{1}{\sigma}\frac{\partial\sigma}{\partial\varepsilon}\bigg|\dot{\varepsilon}+m=1, \tag{1}$$

where $\partial\sigma/\partial\varepsilon$ is the strain hardening modulus and m is the strain rate sensitivity. With the decrease of the strain rate or the increase of the temperature, the deformation mechanism shifts to grain boundary sliding (GBS) and Coble creep, so that m increases monotonically to unity and necking is delayed accordingly. A nonlinear analysis by Hutchinson and Neale [5] gives a more precise relationship between the failure strain, ε_f, and m, which however does not change the above monotonic dependence. The decrease of ε_f with respect to the decrease of the applied strain rate on the left portion of Fig. 1(a) has to result from other mechanisms. Candidate mechanisms include dynamic recrystallization [6], which however occurs at high strain rates and thus does not apply here, and grain growth at low strain rates [7], which however is not widely observed in typical superplastic alloys. As will be presented in this paper, the relationship of $\varepsilon_f \sim \dot{\varepsilon}_{appl}$ at low strain rates is understood by the intergranular failure.

Necking certainly does not apply in the hot forging process. As shown in Fig. 1(b), cylinders with the standard diameter-to-height ratio of 1:2 have been compressed under various temperatures and strain rates to some specific height reduction ratios [8]. These cylinders will experience barreling (which can be reduced upon good

---

[*] Corresponding authors.
E-mail addresses: ygao7@utk.edu (Y. Gao), fengz@ornl.gov (Z. Feng), huangzaiwang@csu.edu.cn (Z. Huang), liangj@ytu.edu.cn (L. Jiang).

https://doi.org/10.1016/j.actamat.2020.04.050
1359-6454/

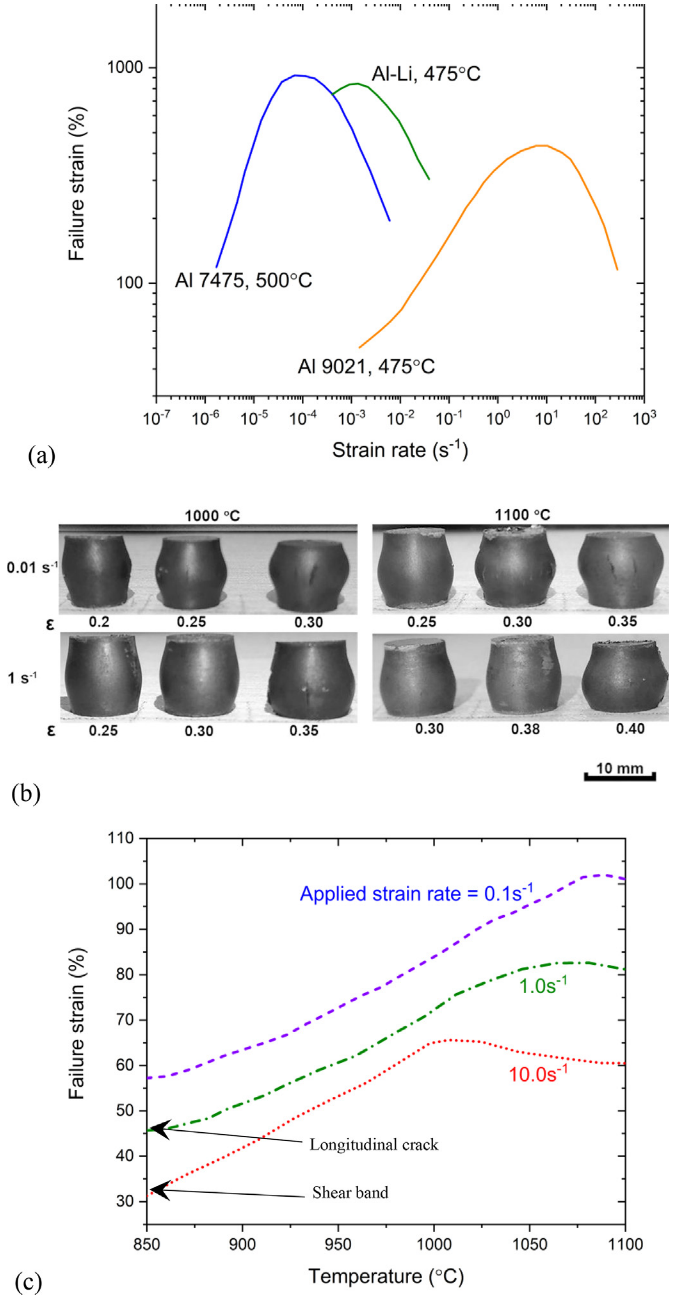

Fig. 1. Representative results of ductility limit versus applied strain rate and temperature in literature. (a) Superplasticity limit (compiled from [3]). (b) Hot forging of Ni-base superalloys (compiled from [8]). (c) Hot compression of Ti alloys (compiled from [10]). Failure modes are known only for the two marked points.

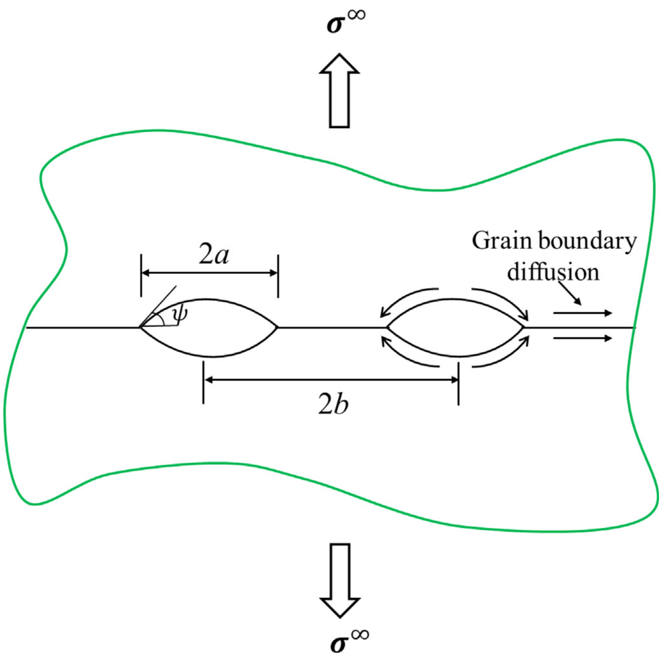

Fig. 2. Schematic illustration of diffusive and creep-constrained growth of grain boundary cavities.

lubrication between platens and the specimen or by no-flat specimen surfaces in Rastegaev upset test) and then longitudinal cracks. The temperature range is too small in these experiments, so that no clear trend with respect to temperature can be identified. The strain-rate increase over two orders of magnitude leads to delayed failure, which is opposite to the dependence of necking instability on the strain rate. Further characterizations reveal that the intergranular cavities be precursors of these longitudinal cracks, and the forging process does not lead to noticeable microstructural changes [9]. It should be noted that a frictionless compression gives a vanishing hoop stress and thus no driving force is provided for grain boundary cavities. On the other hand, although a frictional compression leads to barreling and nontrivial hoop stress, the overall triaxial stress state is still compressive and thus prevents cavity growth. It is not clear on how these two processes jointly or competitively dictate the observed dependence of failure on applied stain rates and temperatures.

Yet the above relationship of $\varepsilon_f \sim \dot{\varepsilon}_{appl}$ in Fig. 1(b) is found to be opposite to the hot-compression tests in Fig. 1(c). In these compression tests of Ti alloys [10], the failure strain ε_f is found to decrease monotonically with the increase of $\dot{\varepsilon}_{appl}$ within the tested ranges of strain rate and temperature. From a closer inspection of the detailed failure processes by the high speed camera, these authors found out the change of failure modes from the longitudinal crack to the shear band, as marked in Fig. 1(c). Therefore, the dependence of longitudinal intergranular cracks on the applied strain may not be opposite to the findings in Fig. 1(b) after all. It goes beyond a reasonable scope of this work to identify the mechanism responsible for the shear band formation in these Ti alloys, but some general shear-banding characteristics can be borrowed from the thermal activation model and numerous works on nanocrystalline and amorphous alloys [11,12].

Summarizing all these experiments in Fig. 1, we can now conclude the following:

- Neck instability is difficult to occur at high temperature and low strain rate, because of the accompanying increase of m. Thus ε_f, if governed by necking, increases with the decrease of $\dot{\varepsilon}_{appl}$ and the increase of T. This partially explains results in Fig. 1(a).
- Our later analysis in this work suggests that the increase of ε_f with respect to the increase of $\dot{\varepsilon}_{appl}$ in Fig. 1(a) and (b) correspond to the delayed growth of grain boundary cavities. A quantitative mechanistic analysis along this line is required because (i) the loading conditions in Fig. 1(a) and (b) are sharply different, (ii) cavity growth can be diffusive or creep-constrained, and (iii) the temperature dependence of ε_f is critically awaited since current experiments in Fig. 1(b) are limited.
- The decrease of ε_f with respect to the increase of $\dot{\varepsilon}_{appl}$ in Fig. 1(c), which is opposite to those in Fig. 1(b), is believed to result from the competition between intergranular crack and shear band. But what causes the initiation of shear band and how this cross-over from one mechanism to the other depends on the environmental temperature are unclear.

Consequently, this work aims to provide a quantitative assessment of the failure strain in intergranular fracture mode in Section 2, and compares its temperature and strain-rate dependence to the necking and shear-band modes. These analyses will help develop the *superplasticity limit diagram* in Section 3, to be compared to Fig. 1(a), and the *forging limit diagram* in Section 4, to be compared to Figs. 1(b) and 1(c). Concluding remarks are given in Section 5.

2. Intergranular cavity growth analysis

We propose that both the monotonically increasing dependence of ε_f on $\dot{\varepsilon}_{appl}$ at low strain rates in Fig. 1(a) and the longitudinal cracks in Fig. 1(b) are governed by the growth of intergranular cavities. Similar to the transition from grain interior dislocation creep to grain boundary diffusional creep as the applied strain rate or stress decrease in the deformation mechanism map [1], the failure mechanism changes from transgranular to intergranular fracture due to the dominance of grain boundary diffusion over lattice diffusion [2,4]. Consider a regular array of cavities on the grain boundary, with the cavity size denoted as $2a$ and the spacing denoted as $2b$ Fig. 2. The balance of surface and interface energies leads to a half dihedral angle of ψ, which remains unchanged during cavity growth due to the rapid surface diffusion process. The volume of the lenticular cavity is

$$V = \frac{4}{3}\pi a^3 h(\psi), \tag{2}$$

whereas the spherical cap shape factor is

$$h(\psi) = \frac{1}{\sin\psi}\left[\frac{1}{1+\cos\psi} - \frac{1}{2}\cos\psi\right]. \tag{3}$$

The area fraction of cavities is given by $f_h = a^2/b^2$.

As first proposed by Hull and Rimmer [13] and later rigorously analyzed by Chuang and Rice [14,15], the diffusive growth rate is governed by the normal stress σ_n,

$$\frac{df_h}{dt} = \frac{2\sigma_n}{\sqrt{f_h}\ln(1/f_h)} \cdot \frac{\Omega}{k_B T} \cdot \frac{1}{b^3 h(\psi)} D_{GB}\delta_{GB}, \tag{4}$$

where D_{GB} is the grain boundary diffusivity, δ_{GB} is the grain boundary thickness, Ω is the atomic volume of the self-diffusing element, k_B is the Boltzmann constant, and T is the absolute temperature. Note that Eq. (4) prescribes a linear dependence on the normal stress. In order to compare this equation to the creep-constrained cavity growth, Cocks and Ashby [16] suggest a rewriting into

$$\frac{1}{\dot{\varepsilon}_0}\frac{df_h}{dt} = \frac{\phi_0}{\sqrt{f_h}\ln(1/f_h)}\left(\frac{\sigma_n}{\sigma_0}\right), \tag{5}$$

$$\phi_0 = \frac{2D_{GB}\delta_{GB}\Omega}{k_B T b^3} \cdot \frac{\sigma_0}{\dot{\varepsilon}_0}, \tag{6}$$

where σ_0 and $\dot{\varepsilon}_0$ are reference parameters in the power-law creep of grain interior. That is,

$$\frac{\dot{\varepsilon}^{GI}_{creep}}{\dot{\varepsilon}_0} = \left(\frac{\sigma_e}{\sigma_0}\right)^n, \tag{7}$$

with σ_e being the Mises effective stress.

The temperature dependence of the power-law creep is represented in the following one-dimensional relationship,

$$\dot{\varepsilon}_{creep} = A\frac{D_L \mu b_{disl}}{k_B T}\left(\frac{\sigma}{\mu}\right)^n, \tag{8}$$

where the lattice diffusion is given by $D_L = D_L^0\exp(-Q_L/RT)$ with R being the gas constant. The grain boundary diffusivity in Eq. (6) is $D_{GB} = D_{GB}^0\exp(-Q_{GB}/RT)$. In these two Arrhenius processes, Q_{GB} and Q_L are the activation energies for the grain boundary diffusion and lattice diffusion, respectively. Taking $\sigma_0 = \mu$, Eq. (6) becomes

$$\phi_0 = \frac{2D_{GB}^0\delta_{GB}}{AD_L^0 b_{disl}} \cdot \frac{\Omega}{b^3}\exp\left(\frac{Q_L - Q_{GB}}{RT}\right). \tag{9}$$

That $Q_{GB} < Q_L$ leads to the decrease of dimensionless ϕ_0 with the increase of T, indicating that a high temperature favor creep dominance.

The competition between the above diffusive process and the creep-constrained growth has been investigated by finite element simulations in Needleman and Rice [17], which defines a dimensionless parameter,

$$L_{NR} = \left[\frac{D_{GB}\delta_{GB}\Omega}{k_B T} \cdot \frac{\sigma_e}{\dot{\varepsilon}^{GI}_{creep}}\right]^{1/3}. \tag{10}$$

Eqs. (6) and (10) are related by

$$\left(\frac{L_{NR}}{b}\right)^3 = \frac{\phi_0}{2}\left(\frac{\sigma_0}{\sigma_e}\right)^{n-1}. \tag{11}$$

A clear physical meaning is borne in Eq. (8), i.e., diffusion dominated ($L_{NR} \gg b$ or $\phi_0 \gg 1$) versus creep governed ($L_{NR} \ll b$ or $\phi_0 \ll 1$) cavity growth. In contrast to ϕ_0, the parameter L_{NR} has an additional stress dependence, from which we find that a stress increase favors creep dominance. These dependences bear significant consequences for the development of high-temperature ductility limit diagrams.

Several approximate models are suggested so as to provide analytical representations of the creep-controlled void growth. Cocks and Ashby [16] give

$$\frac{1}{\dot{\varepsilon}_0}\frac{df_h}{dt} = \beta\left[\frac{1}{(1-f_h)^n} - (1-f_h)\right]\left(\frac{\sigma_e}{\sigma_0}\right)^n, \tag{12}$$

where the dimensionless parameter β is

$$\beta = \sinh\left[-\frac{2\left(n-\frac{1}{2}\right)}{\left(n+\frac{1}{2}\right)}\frac{p}{\sigma_e}\right], \tag{13}$$

and p is the hydrostatic pressure (opposite to the mean stress, σ_m). Detailed finite element simulations in Sham and Needleman [18] and later improvements [19–21] can be fitted to

$$\frac{1}{\dot{\varepsilon}_0} \cdot \frac{df_h}{dt} = f_h\left(\frac{\sigma_e}{\sigma_0}\right)^n \times \begin{cases} \left[\alpha_n\left|\frac{\sigma_m}{\sigma_e}\right| + \beta_n\right]^n \operatorname{sgn}\left(\frac{\sigma_m}{\sigma_e}\right), & \left|\frac{\sigma_m}{\sigma_e}\right| > 1 \\ \left[\alpha_n + \beta_n\right]^n \frac{\sigma_m}{\sigma_e}, & \left|\frac{\sigma_m}{\sigma_e}\right| \le 1 \end{cases} \tag{14}$$

where α_n and β_n are dimensionless fitting parameters that only depend on n.

Failure occurs when f_h increases to a critical value, f_c, often taken as 0.8 as suggested in [17–21]. When the area fraction reaches nearly 80%, the voids are so closely spaced that the void-void junction becomes ligament-like and thus failure occurs by ductile tearing of these ligaments. Therefore, there is no further load bearing capacity, and this particular choice of 80% arises from finite element simulations.

3. Superplasticity limit diagram

3.1. Intergranular cavity growth

Representative analyses are presented here for a ferritic steel with 9.1 wt% Cr, denoted as P91 steel, for which extensive measurements are available such as creep curves and lifetime data over a wide range of applied stresses and temperatures [4,22,23]. Creep and diffusion properties are listed in Table 1. In superplasticity, the stress state is $\sigma_n = \sigma_e$ and $p/\sigma_e = -1/3$. Using Eqs. (5) and (12) and choosing two extreme values of ϕ_0, Fig. 3 plots the cavity growth rates when

Table 1
Material properties for P91 ferritic steel as calibrated in [22,23].

Parameter	Value
Atomic volume, Ω	1.18×10^{-29} m^3
Melting temperature, T_m	1810 K
Lattice diffusion activation energy, Q_L	251 kJ/mol
Reference strain rate for dislocation creep at 650 °C, $\dot{\varepsilon}_0$	1.149×10^{-9} s^{-1}
Reference stress for dislocation creep, σ_0	60 MPa
Stress exponent at 650 °C, n	8
Grain boundary diffusion activation energy, Q_{GB}	174 kJ/mol
Average grain size, d	5 μm

diffusive and creep mechanisms operate separately. As expected, a large (or small) ϕ_0 corresponds to the diffusion (or creep) controlled growth of intergranular cavities.

The cavity growth lifetime, t_f, can be calculated by integrating the sum of Eqs. (5) and (12) with respect to f_h ranging from an initial value, f_i, to a final value, f_c. The latter is taken as 0.8. Due to the logarithmic nature of abscissa in Fig. 3, t_f is insensitive to f_i. The failure strain, ε_f, is given by

$$\varepsilon_f = t_f \dot{\varepsilon}_0 \left(\frac{\sigma_e}{\sigma_0}\right)^n + \frac{4}{3} f_c^{3/2} \frac{b}{d}, \tag{15}$$

in which the first term considers the contribute from grain-interior creep and the second term arises from the presence of cavities that introduces an effective strain by the ratio of the cavity spacing to the grain size. It should be pointed out that the first term is the Monkman–Grant strain, which is indeed not sensitive to temperature at low ϕ_0. It is however not a constant in our predictions.

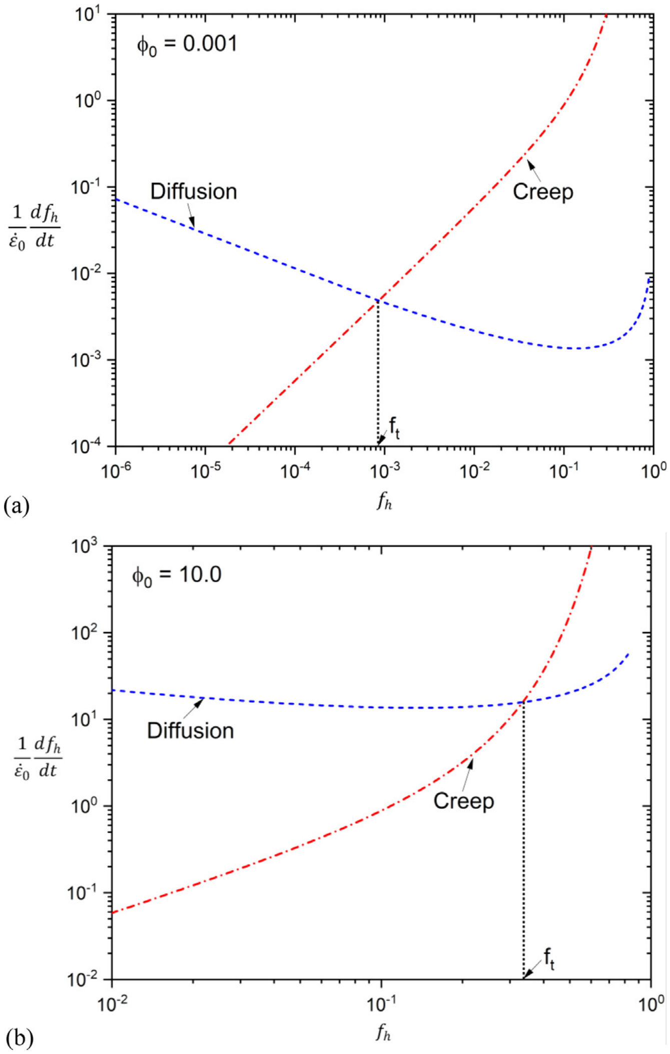

Fig. 3. The cavity growth rate versus the present area fraction of grain boundary cavities. For two representative values of ϕ_0, we have (a) diffusion dominant and (b) creep-controlled behavior, respectively.

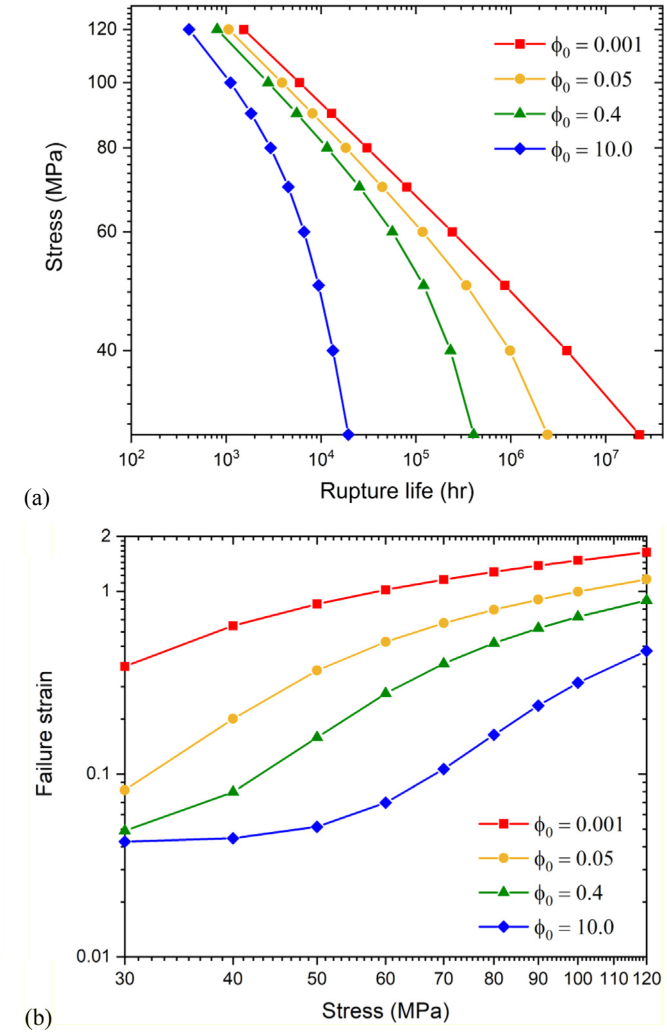

Fig. 4. (a) Stress-lifetime curves, and (b) ductility-stress curves for P91 steels with a wide range of ϕ_0.

The stress-lifetime curves and the ductility-stress curves are plotted in Fig. 4(a) and (b), respectively, for P91 steels with respect to a wide range of ϕ_0. From Eq. (9), we can see that $\phi_0 A b^3/\Omega$ only depends on temperature through an exponential decay, which is plotted in Fig. 5 for several commonly used alloys at elevated temperatures. When $\phi_0 \gg 1$, the cavity growth is diffusion-controlled, so that the rupture lifetime is inversely proportional to the applied stress, which shows a slope of −1 in Fig. 4(a). Also under these circumstances, an extrapolation of the stress-lifetime curve from high stress to low stress is extremely dangerous, since the extrapolation significantly overpredicts the lifetime. This inverse proportionality is reflected as a constant failure strain in Fig. 4(b), e.g., data for ϕ_0=10 and low stresses. When $\phi_0 \ll 1$ or a high temperature, both the lifetime and the failure strain, i.e., t_f and ε_f, increase accordingly.

3.2. Necking analysis

The necking condition in Eq. (1) has two drawbacks when applied to calculate the failure strain. First, for rate dependent solids, the

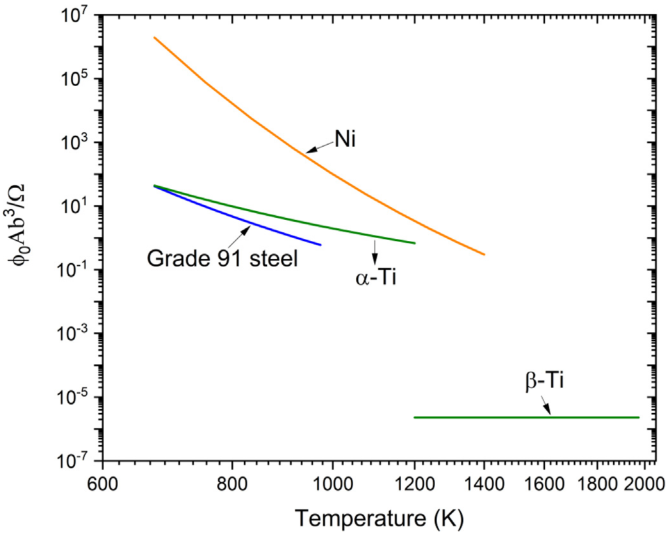

Fig. 5. The dependence of ϕ_0 on temperature as obtained from Eq. (9).

onset of necking is very sensitive to initial geometric perturbation. A one-percent shrinkage of the initial diameter, i.e., η=0.01, may reduce the critical strain for necking by a factor of two. Second, a significant portion of strain can still take place after the onset of necking and before the final failure. A nonlinear analysis by Hutchinson and Neale [5] gives the approximate solution of the failure strain by

$$\varepsilon_f \approx -m\ln\left[1-(1-\eta)^{1/m}\right], \tag{16}$$

as plotted in Fig. 6(a). As expected, when m approaches unity and η vanishes, the ductility in principle goes to infinity.

The strain rate sensitivity in Eq. (16) is that of the entire polycrystal, so the Coble creep should be included in addition to Eq. (7). Using the creep data for P91 steels [4,22,23], Fig. 6(b) plots m against the applied strain rate, which exhibits the rapid change from grain-boundary Coble creep (m=1), to a transitional behavior as dictated by grain boundary sliding, and finally to the grain-interior dislocation creep (e.g., m=1/8 at 650 °C).

3.3. Superplasticity limit diagram and experimental comparisons

Combining the ductility predictions in Figs. 4(b) and 6(a), a superplasticity limit diagram can now be developed in Fig. 7. The family of curves on the right part of this figure are given by the Hutchinson-Neale necking analysis. Because (i) the failure strain under these circumstances is purely governed by $\varepsilon_f(m, \eta)$ and (ii) the dependence of m on the applied strain rate or stress is purely dictated by temperature (i.e., the boundary between dislocation creep and Coble creep in Ashby deformation mechanism maps), this family of curves are marked with different temperature values. On the other hand, the family of curves on the left part of this figure are given with respect to ϕ_0. This parameter is mostly sensitive to temperature as shown in Fig. 5, but it also contains the unknown cavity spacing, b, although a predictive capability without a knowledge of this defect information is impossible.

Results in Fig. 7 compare favorably with the experimental findings in Fig. 1(a). A maximum failure strain is observed for these commercial aluminum alloys, when the applied strain rate varies within 3–4 decades. The right sides of these curves are governed by necking, thus exhibiting steep slopes as the dependence of m on the applied strain rate changes rapidly in the grain boundary sliding regime. In contrast, the left sides of these curves have shallow slopes. In our ductility limit diagram in Fig. 7, both families of curves give comparable predictions of $\varepsilon_f \approx 1$ in intermediate strain rates that correspond to

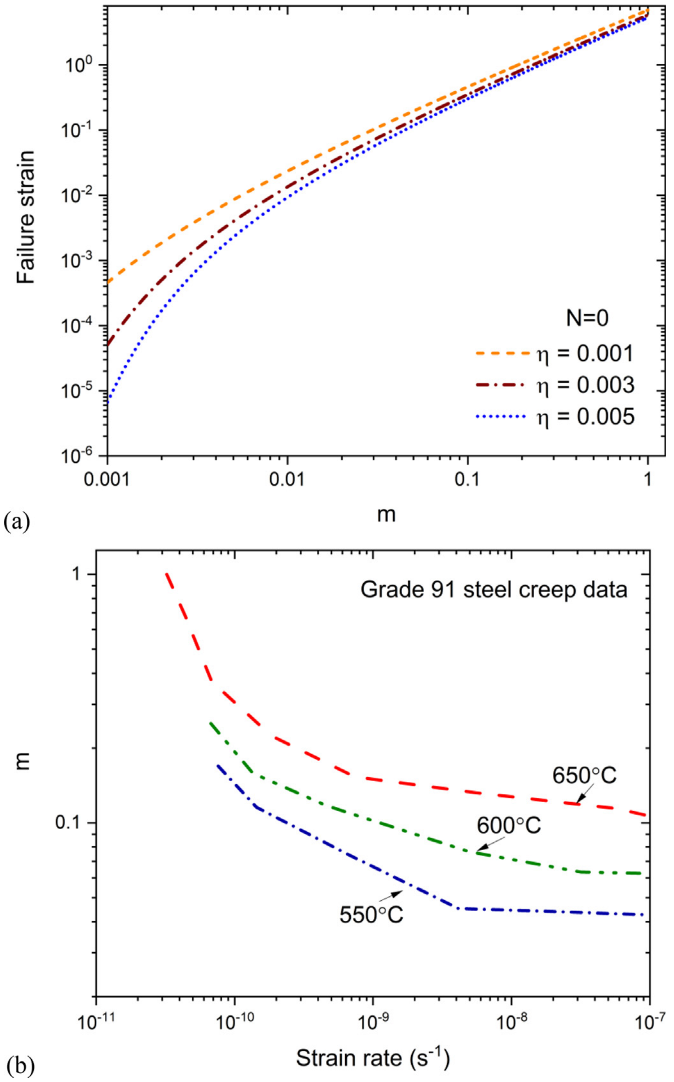

Fig. 6. (a) Ductility in necking analysis. (b) Dependence of the strain rate sensitivity on the applied strain rate for P91 steels (compiled from [4,22,23]).

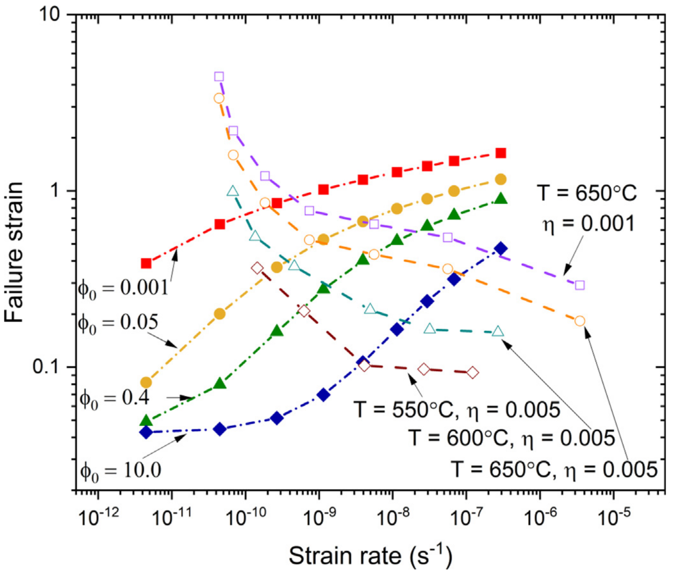

Fig. 7. Superplasticity limit diagram with respect to the applied strain rate for representative values of ϕ_0 (for intergranular fracture) and T and η (for necking).

the grain boundary sliding regime, which provides a reasonable explanation on numerous observations of the connection between superplasticity and GBS. While the Hart condition predicts no favoring over GBS, the intergranular fracture at low strain rates sets a compromise that enables high ductility typically at the GBS regime. A revisit of available experiments and particular their microstructural characterizations is needed for further investigations.

4. Forging limit diagram

4.1. Longitudinal cracks

As briefly mentioned in Section 1, for frictionless compression tests, these cylindrical specimens keep their geometric features. Volume conservation indicates that the plastic strain rate tensor and the deviatoric stress tensor be of the form of

$$\dot{\varepsilon}_p \propto \mathbf{s} \propto \begin{pmatrix} 1 & 0 & 0 \\ 0 & 1 & 0 \\ 0 & 0 & -2 \end{pmatrix}. \tag{17}$$

Therefore, the stress state remains as uniaxial, and there is no hoop stress at the observed longitudinal cracks and thus no driving for these cracks. The friction between platens and these specimens is responsible for the barreling and the nontrivial hoop stress ($\sigma_{\theta\theta}|_{r=R} \neq 0$). The radial stress is zero because of the traction free boundary condition. Consequently, the stress tensor in the shaded regime in Fig. 8 can be written as

$$\sigma^{barrel}\Big|_{r=R} = \begin{pmatrix} 0 & 0 & 0 \\ 0 & \Sigma_{\theta\theta}\sigma_{appl} & 0 \\ 0 & 0 & -(1+\Sigma_{zz})\sigma_{appl} \end{pmatrix}, \tag{18}$$

in which the dimensionless parameters, $\Sigma_{\theta\theta}$ and Σ_{zz}, are small and mainly depend on the friction coefficient between the specimen and platens, and the strain rate sensitivity of the polycrystalline specimen. The stress state is still nearly uniaxial with $\sigma_e \approx \sigma_{appl}$ and $p/\sigma_e \approx 1/3$.

Referring again to Fig. 8, the tensile hoop stress, $\Sigma_{\theta\theta}\sigma_{appl}$, drives the diffusive growth of grain boundary cavities, while the hydrostatic compression leads to the closure of these cavities. Substituting Eq. (18) into Eqs. (5) and (12) gives

$$\frac{1}{\dot{\varepsilon}_0}\frac{df_h}{dt} \approx \frac{\phi_0\Sigma_{\theta\theta}}{\sqrt{f_h}\ln(1/f_h)}\left(\frac{\sigma_{appl}}{\sigma_0}\right) + \beta\left[\frac{1}{(1-f_h)^n} - (1-f_h)\right]\left(\frac{\sigma_{appl}}{\sigma_0}\right)^n, \tag{19}$$

in which the second term is negative because of a positive p/σ_e used in Eq. (13). This equation is now integrated to evaluate the likelihood of intergranular crack under these two opposite processes. As shown by the representative results in Fig. 9, for a given value of $\phi_0\Sigma_{\theta\theta}$, there exists a critical stress above which f_h never exceeds f_c. This observation can be understood from the comparison of the linear dependence on σ_{appl} in the first term of the right hand side of Eq. (19), and the power-law dependence on σ_{appl} in the second term (i.e., n=8 in these calculations). At a large applied stress, the creep-controlled cavity closure always dominates over the hoop-stress-driven diffusive growth of grain boundary cavities.

Rupture lifetime t_f and failure strain ε_f are plotted in Fig. 10 with respect to a wide range of $\phi_0\Sigma_{\theta\theta}$ for P91 steels. Note that t_f is calculated by integrating Eq. (19) as that in Section 3, but the calculation of ε_f differs significantly from Eq. (15). The failure strain is the zz-component,

$$\varepsilon_{zz}^{failure} = t_f\dot{\varepsilon}_{zz}^{creep}, \tag{20}$$

which does not include the second term in Eq. (15) since these cavities contribute to the hoop strain but not to the longitudinal strain. Also the strain rate used in Eq. (20) is a sum of the dislocation creep and Coble creep mechanisms again because of the zz-component used here. At low stresses or strain rates, since the failure is governed by the hoop-stress-driven diffusive growth of grain boundary cavities, the lifetime is found to inversely proportional to the applied stress in Fig. 10(a). If $\dot{\varepsilon}_{zz}^{creep}$ is still governed by dislocation creep, the slope in the double-logarithmic plot of $\varepsilon_f \sim \sigma_{appl}$ at low applied stresses is $n-1$. However, at low strain rates, $\dot{\varepsilon}_{zz}^{creep}$ tends to be dictated by Coble creep under which the relationship between stress and strain rate is linear, so that Fig. 10(b) shows the same inversely proportional relationship to the applied strain rate at low strain rates, and Fig. 10(c) shows a nearly constant strain at low strain rates. The temperature dependence is the same as that in Fig. 4(b). That is, a temperature increase leads to a decrease of ϕ_0, and thus an increase in ductility in Fig. 10(c).

4.2. Experimental comparisons

It is commonly believed that high temperature processing techniques tend not to encounter failure with the increase of processing temperature and the decrease of applied strain rate. This is true for necking, but not true for intergranular cracks under uniaxial tension in Section 3. For the hot-forging experiments on Ni-base superalloys [8] in Fig. 1(b), the trend is again opposite. An increase of the applied strain rate is beneficial, which agrees nicely with our predictions in Fig. 10(b). The temperature dependence is rather unclear, because a mere change of temperature from 1000 °C to 1100 °C only leads to a small change of ϕ_0 provided with the same b (which rather depends on prior thermomechanical treatments and is thus unknown).

For the hot compression tests on Ti alloys [10] in Fig. 1(c), the temperature dependence is the same as the prediction in Fig. 10(b), but the strain rate dependence is opposite to our prediction, as well as to the findings in Fig. 1(b). Using a high speed camera, these authors [10] found out the change of the failure mode from the longitudinal crack (850 °C and 1 s^{-1}) to the shear band (850 °C and 10 s^{-1}). Unfortunately, their compiled results of ε_f with respect to temperature and applied strain rate were not labeled with the corresponding failure mode (only two data points in Fig. 1(c) can be read from their paper). Nevertheless, it is rather known that the shear banding behavior shows the same dependence on temperature and applied strain rate as for the necking condition, as rationalized below.

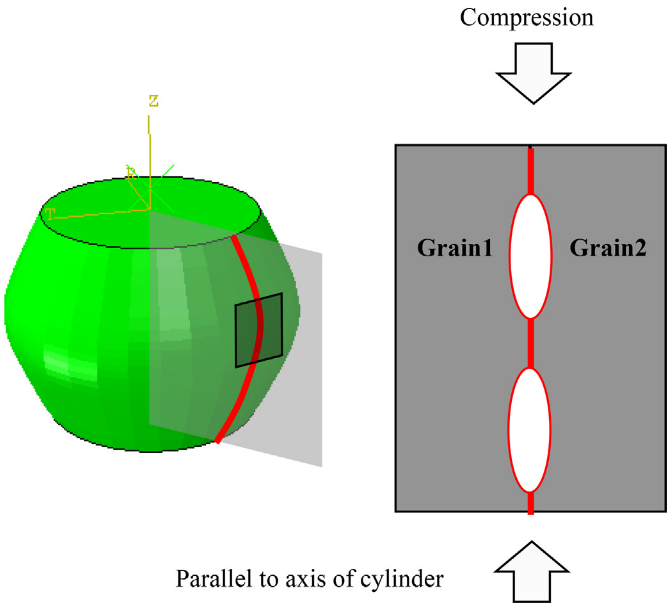

Fig. 8. Hot forging leads to barreling and non-zero hoop stress that is responsible for longitudinal cracks.

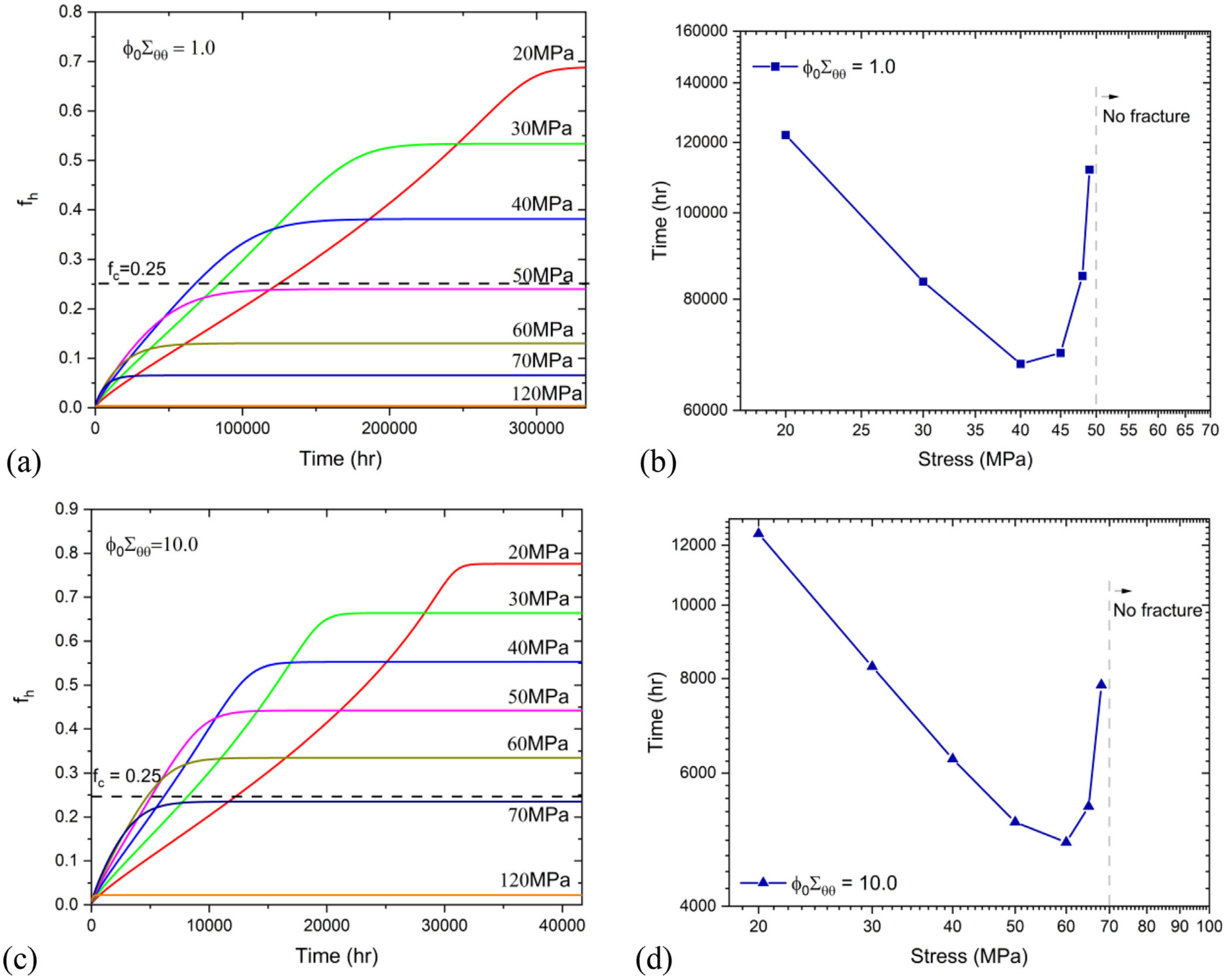

Fig. 9. The evolution of area fraction of cavities and the corresponding lifetime with respect to various stress levels in (a)/(c) and (b)/(d), respectively. (a) and (b): $\phi_0\Sigma_{\theta\theta}$=1. (c) and (d): $\phi_0\Sigma_{\theta\theta}$=10.

Strain localization, whether into the shear direction or off the shear direction, can be understood as a constitutive instability. The terminology of shear band is used when the localized band is along or slight off the shear direction, while dilatational/compaction bands are used when the localized band is almost orthogonal to the shear direction [24–26]. For rate-independent solids, a homogeneous deformation becomes unstable at a critical condition, most commonly due to strain softening, yield surface vertices, and pressure dependence. This process is sudden and catastrophic. For rate-dependent solids, it is the spectral growth rate of various defects that dictate the shear banding behavior. The growth of initial defects or perturbations is controlled by one or several thermally activated processes. These processes are of the Arrhenius nature; that is, when approaching the athermal limit (either low temperature or high strain rate), there is little time for these processes to take place, and thus shear bands easily appear and the overall ductility is low. Away from the athermal limit (i.e., at either high temperature or low strain rate), any fluctuations can be easily smeared out and failure can thus be delayed. In other words, the shear-banding behavior and the necking condition have the same dependence on temperature and applied strain rate, but for different reasons (shear-banding being away from the athermal limit, and necking seeking a high m).

4.3. Forging limit diagram

Combining results in Fig. 10 and the above discussion on strain localization in rate-dependent solids, we now prescribe the forging limit diagram in Fig. 11. As it is infeasible to derive a quantitative prediction based on shear bands, the corresponding ductility limit is only schematically illustrated. When applying this diagram to actual experiments, we also note that $\Sigma_{\theta\theta}$ can also be varied easily in experiments.

5. Concluding remarks

As opposed to the common belief that a high temperature and/or a low applied strain rate will prevent the failure in high temperature processing, we find that the failure strain has a far more complicated dependence on these loading parameters. For uniaxial tensile tests, we determine the corresponding failure strain with respect to intergranular fracture (diffusion-controlled or creep-constrained) and necking, and the resulting superplasticity limit diagram compares favorably to experiments complied in [3] and Fig. 1(a). For uniaxial compression tests, barreling is a necessary condition for the longitudinal fracture. The competition between hoop-stress-induced diffusional growth and creep-induced closure of grain boundary cavities,

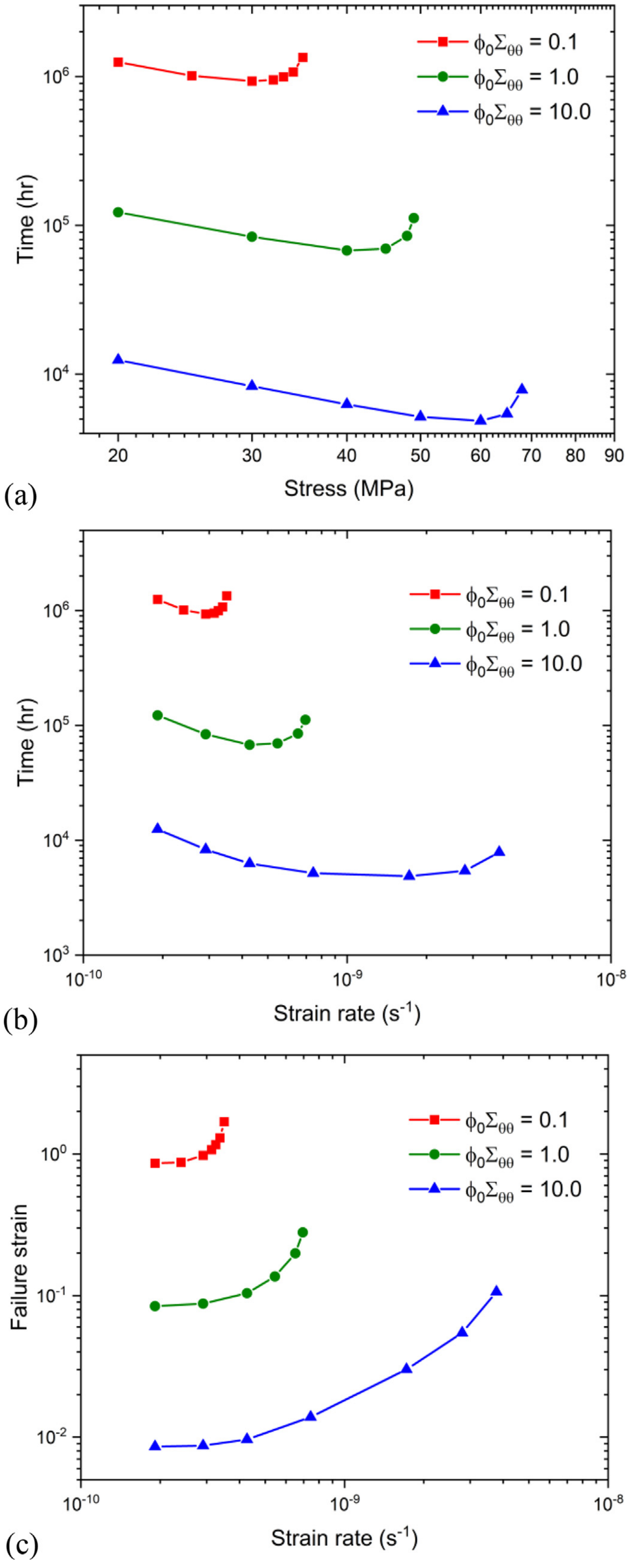

Fig. 10. (a) Rupture lifetime against the applied stress, (b) rupture lifetime against the applied strain rate, and (c) rupture strain against the applied strain rate for P91 steels (parameters in Table 1) under the forging condition in Fig. 8.

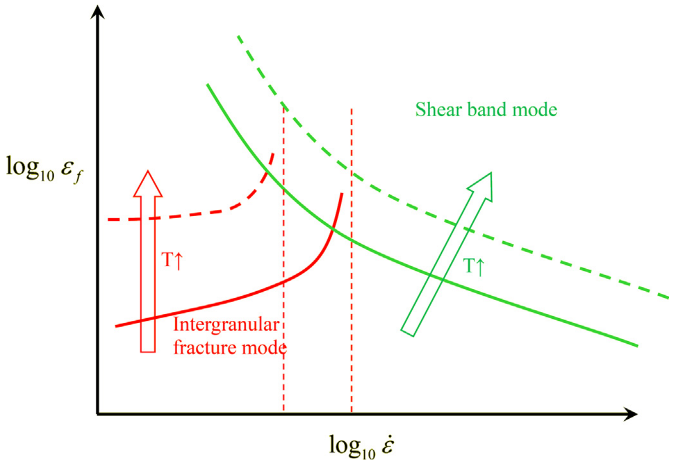

Fig. 11. Schematic illustration of the forging limit diagram.

together with the likely appearance of shear bands, dictate a forging limit diagram, which compares favorably experiments in Fig. 1(b) [8] and (c) [10]. However, further investigations are needed for these experiments, especially on the extension of their parametric space and on the careful identification of failure modes. These two types of ductility limit diagrams provide critical insights in the design of many high temperature processing techniques. Finally, we note that our results are based on individual cavities, while a more complete and accurate prediction requires a finite element simulation of collective behavior of cavities (such as by the smear-out model in [19–23]).

Declaration of Competing Interest

None.

Acknowledgments

The authors are grateful to financial support from the U.S. Department of Energy, Office of Vehicle Technology for the work performed at Oak Ridge National Laboratory, from the U.S. National Science Foundation (DMR-1809640) for the work at University of Tennessee, and from the National Key Research and Development Program of China (2016YFB0700300) for the work at Central South University. YFG acknowledges fruitful discussions with Prof. T.G. Nieh at University of Tennessee and Dr. T.L. Sham at Argonne National Laboratory.

Supplementary materials

Supplementary material associated with this article can be found in the online version at doi:10.1016/j.actamat.2020.04.050.

References

[1] H.J. Frost, M.F. Ashby, Deformation-Mechanism Maps: The Plasticity and Creep of Metals and Ceramics, Pergamon Press, 1982.
[2] H. Riedel, Fracture at High Temperatures, Springer-Verlag, 1986.
[3] T.G. Nieh, J. Wadsworth, O.D. Sherby, Superplasticity in Metals and Ceramics, Cambridge University Press, 1997.
[4] F. Abe, T.U. Kern, R. Viswanathan, Creep-Resistant Steels, Elsevier, 2008.
[5] J.W. Hutchinson, K.W. Neale, Influence of strain-rate sensitivity on necking under uniaxial tension, Acta Metall. 25 (1977) 839–846.
[6] T.G. Nieh, L. Hsiung, J. Wadsworth, R. Kaibyshev, High strain rate superplasticity in a continuously recrystallized Al–6%Mg–0.3%Sc alloy, Acta Mater. 46 (1998) 2789–2800.
[7] T.G. Langdon, Grain boundary sliding revisited: developments in sliding over four decades, J. Mater. Sci. 41 (2006) 597–609.
[8] G. He, F. Liu, L. Huang, L. Jiang, Analysis of forging cracks during hot compression of powder metallurgy nickel-based superalloy on simulation and experiment, Adv. Eng. Mater. 18 (2016) 1823–1832.

[9] X. Wang, Z. Huang, B. Cai, N. Zhou, O. Magdysyuk, Y.F. Gao, S. Srivatsa, L. Tan, L. Jiang, Formation mechanism of abnormally large grains in a polycrystalline nickel-based superalloy during heat treatment processing, Acta Mater. 168 (2019) 287–298.

[10] Y. Zhu, W. Zeng, F. Zhang, Y. Zhao, X. Zhang, K. Wang, A new methodology for prediction of fracture initiation in hot compression of Ti40 titanium alloy, Mater. Sci. Eng. A 553 (2012) 112–118.

[11] J.R. Trelewicz, C.A. Schuh, The Hall-Petch breakdown in nanocrystalline metals: a crossover to glass-like deformation, Acta Mater. 55 (2007) 5948–5958.

[12] C.J. Su, J.A. LaManna, Y.F. Gao, W.C. Oliver, G.M. Pharr, Plastic instability in amorphous selenium near its glass transition temperature, J. Mater. Res. 25 (2010) 1015–1019.

[13] D. Hull, D.E. Rimmer, The growth of grain boundary voids under stress, Philos. Mag. 4 (1959) 673–687.

[14] T.J. Chuang, J.R. Rice, The shape of intergranular creep cracks growing by surface diffusion, Acta Metall. 21 (1973) 1625–1628.

[15] T.J. Chuang, K.I. Kagawa, J.R. Rice, L.B. Sills, Non-equilibrium models for diffusive cavitation of grain interfaces, Acta Metall. 27 (1979) 265–284.

[16] A.C.F. Cocks, M.F. Ashby, On creep fracture by void growth, Prog. Mater. Sci. 27 (1982) 189–244.

[17] A. Needleman, J.R. Rice, Plastic creep flow effects in the diffusive cavitation of grain boundaries, Acta Metall. 28 (1980) 1315–1332.

[18] T.L. Sham, A. Needleman, Effects of triaxial stressing on creep cavitation of grain boundaries, Acta Metall. 31 (1983) 919–926.

[19] V. Tvergaard, Material failure by void growth to coalescence, Adv. Appl. Mech. 27 (1990) 83–151.

[20] E. van der Giessen, V. Tvergaard, Development of final creep failure in polycrystalline aggregates, Acta Metall. Mater. 42 (1994) 959–973.

[21] P. Onck, E. van der Giessen, Growth of an initially sharp crack by grain boundary cavitation, J. Mech. Phys. Solids 47 (1998) 99–139.

[22] W. Zhang, X. Wang, Y.Y. Wang, X.H. Yu, Y.F. Gao, Z.L. Feng, Type IV failure in weldment of creep resistant ferritic alloys: I. Micromechanical origin of creep strain localization in the heat affected zone, J. Mech. Phys. Solids 134 (2020) 103774.

[23] W. Zhang, X. Wang, Y.Y. Wang, X.H. Yu, Y.F. Gao, Z.L. Feng, Type IV failure in weldment of creep resistant ferritic alloys: II. Creep fracture and lifetime prediction, J. Mech. Phys. Solids 134 (2020) 103775.

[24] J.W. Rudnicki, J.R. Rice, Conditions for the localization of deformation in pressure-sensitive dilatant materials, J. Mech. Phys. Solids 23 (1975) 371–394.

[25] Y.F. Gao, L. Wang, H. Bei, T.G. Nieh, On the shear-band direction in metallic glasses, Acta Mater. 59 (2011) 4159–4167.

[26] M.Q. Jiang, G. Wilde, J.H. Chen, C.B. Qu, S.Y. Fu, F. Jiang, L.H. Dai, Cryogenic-temperature-induced transition from shear to dilatational failure in metallic glasses, Acta Mater. 77 (2014) 248–257.